Inorganic Chemistry

Article

pubs.acs.org/IC

Metastable (Bi, M)$_2$(Fe, Mn, Bi)$_2$O$_{6+x}$ (M = Na or K) Pyrochlores from Hydrothermal Synthesis

Luke M. Daniels,[†] Helen Y. Playford,[‡] Jean-Marc Grenèche,[§] Alex C. Hannon,[‡] and Richard I. Walton*[,†]

[†]Department of Chemistry, University of Warwick, Gibbet Hill Road, Coventry CV4 7AL, United Kingdom

[‡]ISIS Facility, Rutherford Appleton Laboratory, Didcot, Oxford OX11 0QX, United Kingdom

[§]Institut des Molécules et des Matériaux du Mans, UMR 6283—CNRS LUNAM Université du Maine, 72085 Le Mans, France

Supporting Information

ABSTRACT: The hydrothermal syntheses, structures, and magnetism of two new pyrochlore oxides of compositions $(Na_{0.60}Bi_{1.40})(Fe_{1.06}Mn_{0.17}Bi_{0.77})O_{6.87}$ and $(K_{0.24}Bi_{1.51})(Fe_{1.07}Mn_{0.15}Bi_{0.78})O_{6.86}$ are described. With preparation at 200 °C for 6 h in solutions of sodium or potassium hydroxide, the alkali metals introduced from these mineralizers are essential to the synthesis of the phases. The average long-range order of the pyrochlore structure, with space group $Fd\bar{3}m$, was investigated and refined against X-ray and neutron diffraction data, and it was shown that disorder is present in both the metal and coordinating oxygen positions, along with metal-mixing across both the A and B sites of the structure. XANES analysis confirms the presence of Mn^{4+}, mixed valence Bi^{3+} and Bi^{5+}, and Fe^{3+}, the last also verified by ^{57}Fe Mössbauer spectroscopy. Magnetic measurements show a lack of long-range magnetic ordering that is typical of geometrically frustrated pyrochlores. The observed glasslike interactions occur at low temperatures, with the onset temperature depending upon the magnitude of the applied external field. Variable temperature X-ray diffraction shows that these pyrochlores are metastable and collapse on heating at ca. 395 °C, which suggests that their formation by conventional solid-state synthesis would be impossible.

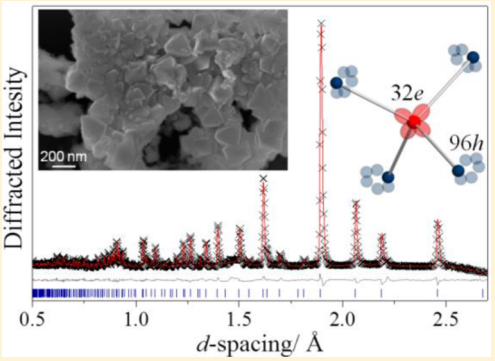

INTRODUCTION

Pyrochlore oxides ideally adopt the symmetry of the cubic space group $Fd\bar{3}m$ with eight formula units of $A_2B_2O_6O'$ enclosed within each unit cell. The pyrochlore structure is found for various combinations of eight-coordinated A-site and six-coordinated B-site metals.[1] In the ideal crystal structure there are only four crystallographic sites that are occupied, usually defined as 16*d* ($^1/_2$, $^1/_2$, $^1/_2$), 16*c* (0, 0, 0), 48*f* (x, $^1/_8$, $^1/_8$), and the 8*b* ($^3/_8$, $^3/_8$, $^3/_8$), which correspond to the A, B, O, and O′ atoms, respectively. Nevertheless, the pyrochlore structure can accommodate high levels of structural disorder of various types, often leading to interesting properties. The O′ site, for example, can be partially occupied or completely unoccupied to give $A_2B_2O_6$ in extreme cases, allowing for the formation of many different mixed-valence pyrochlores.[2] It is also possible for the O′ site to be occupied by other anionic species such as halides or hydroxides, or even neutral species such as water.[1] The potential for disorder is not only limited to the oxygen sublattice, with vacancies on the A site also tolerated to give compositions of $A_{2-x}B_2O_{7-y}$, and it is common for some metals to mix across both the A and B sites.[3] Further disorder can be introduced into the A_2O' network particularly when cations with stereochemically active lone pairs of electrons such as Pb^{2+}, Sn^{2+}, or Bi^{3+} reside on the A site. The lone pair often causes the metal atoms to be off-center from the ideal position, and the displaced position is commonly modeled using the 96*h* Wyckoff position. This can generate distortion in the local oxygen environment surrounding the A site shifting the O′ anion away from the 8*b* and onto the 32*e* position.[4]

The hydrothermal method is a useful synthetic route for many oxides and other materials, and the production of pyrochlores has been increasingly reported from such low-temperature solution crystallizations, without the need of high temperatures usually associated with preparative solid-state chemistry.[5] Hydrothermal synthesis can be used for the formation of stoichiometric pyrochlores such as $Ca_2M_2O_7$ (where M = Nb and Ta);[6] however, it can also give rise to the production of novel and complex phases whose structures contain metals in unusual oxidation states. For example, the pyrochlores $(Na_{0.33}Ce_{0.67})_2Ti_2O_7$ and $KLuTa_2O_7$ are produced hydrothermally and are metastable in that they phase separate on heating, showing that they cannot be produced through traditional solid-state synthesis techniques.[7] The hydrothermal chemistry of bismuth-containing oxides has been explored with the production of several different pyrochlores such as $Bi_{1.43}Ti_2O_6(OH)_{0.29}(H_2O)_{0.66}$,[8] $Na_{0.32}Bi_{1.68}Ti_2O_{6.46}(OH)_{0.44}$,[9] and $M_2Sn_2O_7$ (where M = La, Bi, Gd, or Y).[10] Hydrothermal synthesis of bismuth oxides has often resulted in pyrochlore phases that contain Bi^{3+} and Bi^{5+} on the A and B sites of the structure, respectively. For example, the materials $(K_{1.14}Bi_{0.37}{}^{3+}\square_{0.49})(Bi_{0.27}{}^{3+}Bi_{1.73}{}^{5+})O_{5.7}(OH)_{0.3}$ and

Received: October 2, 2014
Published: November 21, 2014

$(Na_{0.39}Bi_{1.45}^{3+}\square_{0.16})(Bi_{0.37}^{3+}Bi_{1.63}^{5+})O_7$ (where $\square$ represents a cation vacancy) were prepared from Bi^{3+} and Bi^{5+} reagents, respectively, suggesting it is likely that the mild chemistry also influences resulting oxidation states.[11]

Many bismuth-containing pyrochlores have potentially valuable properties. For example, Bi_2InNbO_7 has a tunable band gap upon substitution of In^{3+} for Fe^{3+}, causing it to exhibit photocatalytic behavior under UV radiation.[12] In thin film form, $Bi_2Ti_2O_7$, with high permittivity and low leakage current, has been used to improve the electrical properties of the ferroelectric Aurivillius phase of $Bi_4Ti_3O_{12}$.[13,14] Among the most widely studied bismuth-containing pyrochlores are $(Bi,Zn)_2(Zn,Nb)_2O_7$ ceramics, which possess high dielectric constants with low loss, useful properties that suggest a potential for use in high-frequency multilayer capacitors.[15] It has been shown that the further the Bi^{3+} cation is displaced away from the ideal 16*d* site, then the greater the dielectric constant of the material is,[16] without any significant degradation of dielectric loss.[17] Krayzman et al. used a combination of EXAFS and bond valence analysis to show that these dielectric properties are intimately linked with the static disorder caused by Bi^{3+} off-centering.[18] Through careful modeling it was indicated that the displacement of the O′ anion is directed toward coordinating Zn^{2+} cations and away from Bi^{3+} cations.

Interestingly, pyrochlores containing magnetic metal cations have geometrically and chemically frustrated magnetism, which can often present itself as glassy-type behavior. The disorder introduced into the A_2O' network from the bismuth as well as the random distribution of transition metals across both the A and B sites lead to frustrated magnetic states in several bismuth and iron containing pyrochlores, such as $(Bi_{1.89}Fe_{0.11})(Fe_{1.05}Nb_{0.95})O_7$ and $(Bi_{1.88}Fe_{0.12})(Fe_{1.42}Te_{0.58})O_{6.87}$.[19] Occasionally the mixture of metals produces both ferro- and antiferromagnetic interactions, and the interplay between these results in the absence of long-range magnetic ordering.[20]

In this Article we describe the formation of two new metastable mixed Bi, Fe, and Mn disordered pyrochlore oxides from the hydrothermal reaction of bismuth, iron, and manganese reagents in concentrated alkali metal hydroxide solutions. While the hydrothermal synthesis of the perovskite $BiFeO_3$ has been reported,[21] and the hydrothermal formation of the bismuth manganese material $Bi_3Mn_4O_{12}(NO_3)$ has been described,[22] we show that by combining iron and manganese salts, with the aim of preparing oxides with interesting magnetic properties, the formation of complex pyrochlore phases is achieved. Their average crystal structure is solved using Rietveld refinement, and the results are compared with data from several complementary techniques. Data from magnetic measurements of the frustrated glassy-type pyrochlore materials are also reported.

EXPERIMENTAL METHODS

Synthesis. Hydrothermal reactions were performed in Teflon-lined stainless-steel autoclaves with internal volumes of approximately 20 mL. Sodium bismuthate(V) dihydrate (85% Acros Organics), iron(III) nitrate nonahydrate (98%+ ACS reagent grade), and manganese(II) chloride tetrahydrate (99% Alfa Aesar) were dissolved into 8 mL of ultrapure water to give a Bi:Fe:Mn molar ratio of 1:0.5:0.1. The level of hydration of the starting materials had been previously verified using thermogravimetric analysis (TGA). Pellets of sodium or potassium hydroxide (analytical grade) of sufficient quantity to give a concentration of 4.0 M were added to the solutions with stirring for 15 min, before they were sealed inside the autoclaves and placed in preheated forced-air ovens (Genlab MINO/40) at 200 °C for a period of 6 h, before being removed and allowed to cool naturally to room temperature. The brown polycrystalline powders obtained were washed with deionized water several times and collected by suction filtration before being dried at 75 °C in air.

Characterization. X-ray diffraction (XRD) patterns for phase identification were collected using a Siemens D5000 diffractometer equipped with bichromatic Cu $K\alpha_{1/2}$ radiation. High resolution powder XRD data were collected using a Panalytical X'Pert Pro MPD equipped with monochromatic Cu $K\alpha_1$ radiation and a PIXcel solid-state detector.

Time-of-flight neutron diffraction data were collected using the General Materials diffractometer (GEM) at ISIS, the U.K. spallation neutron source.[23] The powders were placed into thin-walled vanadium cylindrical cans of inner diameter 0.6 cm with wall thickness of 0.004 cm. To minimize the effect of incoherent scatter by hydrogen, all samples were synthesized in D_2O, and any residual moisture was driven off from the powders under reduced pressure in a ThermoScientific Heraeus Kelvitron T vacuum oven at 80 °C before the cans were placed in the neutron beam. To achieve high statistical quality, data were recorded for 6 h from each sample. Data collected from an empty vanadium can, the empty instrument, and a solid vanadium rod of 0.834 cm diameter were used to normalize the raw data through the correction program GudrunN.[24]

Simultaneous Rietveld refinements against both the powder XRD and the time-of-flight data were performed using the program TOPAS-Academic (Version 4.1) implemented with jEdit (Version 4.3.1).[25] Data from banks 3, 4, and 5 (mean scattering angles of 35.14°, 62.39°, and 92.83°, respectively) of GEM were included in these refinements with bank 3 providing modest resolution and a sufficiently large *d*-spacing range to include the 111 reflection in the refinement, while the higher-angle bank 5 offers increased resolution of the lower *d*-spacing peaks.[26]

Densities of the polycrystalline powders were measured using a Quantachrome Micropycnometer. Identical preparation conditions to the neutron scattering measurements were used whereby the samples were placed in a vacuum oven at 80 °C to drive off residual moisture before measurement. The powders were purged under a constant flow of helium for 15 min, and measurements were taken until six consecutive pressure readings (P_1/P_2) had stabilized within agreement of 0.001.

The relative compositions of the metals present in the pyrochlores were determined accurately using inductively coupled plasma optical emission spectroscopy (ICP-OES) by the company MEDAC Ltd. (U.K.).

X-ray fluorescence (XRF) spectroscopy was performed using a Panalytical Epsilon 3^{XL} energy dispersive X-ray fluorescence spectrometer with an X-ray tube operating at 50 kV and a silicon drift detector.

Nonambient XRD measurements were made using a Bruker D8 Advance diffractometer equipped with bichromatic Cu $K\alpha_{1/2}$ radiation and a VÅNTEC-1 high-speed detector. Powders were heated *in situ* using a Anton Paar XRK 900 reaction chamber controlled through a TCU 750 temperature unit.

Thermogravimetric analysis (TGA) was performed using a Mettler Toledo Systems TGA/DSC 1 instrument under a constant flow of air (50 mL/min). Differential scanning calorimetry (DSC) curves were also recorded. Data were recorded from room temperature up to 1000 °C at a rate of 10 °C/min.

X-ray absorption near-edge spectroscopy (XANES) data were measured in transmission mode on beamline B18 at the Diamond Light Source.[27] Pellets were prepared by grinding ∼12 mg of the pyrochlore into ∼80 mg of polyethylene powder before being pressed into 13 mm diameter pellets of thickness ∼1 mm. Data were recorded across the K-edge energies of Fe and Mn, and the L_{III}-edge of Bi. Normalization of the data was performed by subtracting linear pre-edge and polynomial postedge backgrounds using the software Athena.[28]

^{57}Fe Mössbauer spectrometry was performed using a conventional constant acceleration transmission spectrometer, with a ^{57}Co radio-

dx.doi.org/10.1021/ic502411z | Inorg. Chem. 2014, 53, 13197−13206

active source diffused into a Rh matrix. Spectra were recorded at 300 and 77 K using a bath cryostat, and were fitted using the MOSFIT program[29] with and/or quadrupolar doublets based on lines with Lorentzian profiles. An α-Fe foil was used as the calibration sample, and the isomer shift values are quoted relative to that of α-Fe at 300 K.

For transmission electron microscopy (TEM), powders were ultrasonically dispersed in methanol before being placed onto a lacy carbon film reinforced on a copper grid. Images were obtained using a JEOL 2100 LaB_6 instrument operating at 200 kV. Scanning electron microscopy (SEM) images were recorded using a Zeiss SUPRA 55VP FEG instrument with a working distance of 3 mm.

Magnetization data for each pyrochlore were recorded using a Quantum Design MPMS-5S SQUID magnetometer over a temperature range 2−400 K. Zero field-cooled warming (ZFCW) and field-cooled cooling (FCC) data were collected while magnetic fields of various magnitudes were applied. Remanent magnetization (RM) curves were recorded after collecting the FCC data. The material was cooled in the presence of an applied field, and the field was then set to zero before collecting magnetization data on warming.

RESULTS AND DISCUSSION

Structure. Powder XRD, Figure 1, shows that phase-pure cubic pyrochlore oxides (space group $Fd\bar{3}m$) have been successfully produced from hydrothermal synthesis, while elemental analysis (Table 1) shows them to contain bismuth, iron, and manganese, as well as alkali metals from the hydroxides used in the synthesis. To the best of our knowledge, this is the first time that such combinations of metals have been reported in the pyrochlore structure. The optimal synthesis conditions for the formation of these phases were found to be 4.0 M aqueous hydroxide at 200 °C for 6 h; solution concentrations and reaction temperatures above or below 4.0 M and 200 °C, respectively, as well as synthesis durations longer than 6 h lead to the formation of impurity phases such as $BiFeO_3$ and sillenite ($Bi_{12}MnO_{20}$ or $Bi_{25}FeO_{40}$).

The use of equimolar ratios of iron and manganese in the syntheses proved unsuccessful, also giving impurity phases. The ideal molar ratio between bismuth, iron, and manganese reactants was found to be 1:0.5:0.1, respectively. If the amount of manganese was increased (e.g., to 1:0.5:0.5), this resulted in the postreaction filtrate being intensely green in color, suggesting that excess manganese remains in solution as the MnO_4^{2-} manganate(VI) ion. This excess of Mn also introduces a sillenite impurity phase, indicating that there is a limit to the concentration of manganese in these pyrochlores.

The use of NaOH or KOH as mineralizer results in the production of different pyrochlore phases, evidenced by a larger lattice parameter of a = 10.70849(12) Å for the potassium containing pyrochlore compared with a = 10.6947(3) Å for the sodium containing pyrochlore. This is consistent with the presence of the larger K^+ ion in the structure, with K^+ and Na^+ having ionic radii of 1.51 and 1.18 Å, respectively (VIII coordinate environment).[30] The presence of the alkali metals was confirmed through elemental analysis which also provides information about the relative amounts of other metals. The results from ICP-OES and XRF analysis are given in Table 1 and are compared with those obtained from Rietveld refinement of XRD and neutron data. The values obtained from ICP-OES and XRF are very similar, the only discrepancy being that of sodium, for which XRF gives a much lower value. This is not unexpected since Na fluorescence is on the lower limit of the detectable energy range of the instrument. Though the XRF value for Na is not quantitative, it confirms the presence of the metal in the structure, and henceforth, the pyrochlores are referred to as "Na pyrochlore" or "K pyrochlore" signifying which alkali metal is present. These results suggest that the alkali metals are necessary to the synthesis to allow the formation of the pyrochlore structure. This was explored further by performing the synthesis using ammonium hydroxide as mineralizer. These attempts did not result in the formation of a pyrochlore phase (see Supporting

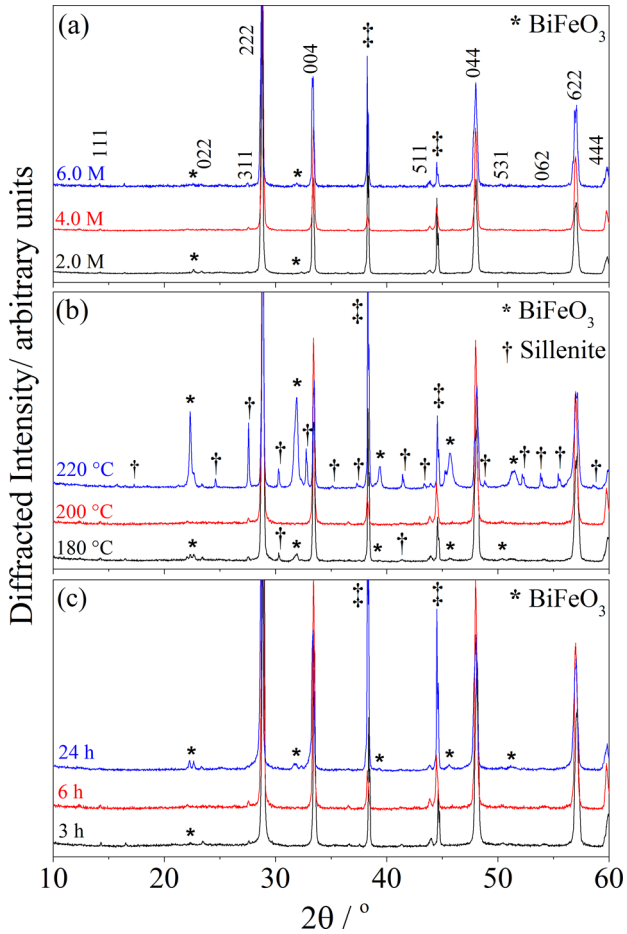

Figure 1. Powder XRD of the Na pyrochlore only, showing the effect of various reaction conditions on the synthesis of the pyrochlore materials. Panel (a) shows how the concentration of mineralizer solution at 200 °C for 6 h influences the end product, panel (b) highlights how the variation in reaction temperature changes the outcome of the reaction in 4 M solutions for 6 h, and panel (c) displays different synthesis durations of 4 M solutions at 200 °C. Almost identical impurities are obtained for the K pyrochlore under these conditions. The symbol ‡ signifies reflections from the aluminum sample holder.

Table 1. Elemental analysis for all the metals present in the pyrochlore materials from ICP-OES and XRF measurements and comparison with the composition refined from diffraction data

element/at. %	Bi	M (Na or K)	Fe	Mn
Na Pyrochlore				
ICP-OES	53.87	12.51	27.99	5.63
XRF	56.59	5.82	31.15	6.44
refined	54.18	14.89	26.66	4.27
K Pyrochlore				
ICP-OES	60.62	4.89	30.41	4.06
XRF	60.62	4.75	30.74	3.88
refined	61.15	6.38	28.49	3.97

dx.doi.org/10.1021/ic502411z | Inorg. Chem. 2014, 53, 13197−13206

Information Figure S1), which supports the postulate that the alkali metals are included in the pyrochlore structure.

Simultaneous Rietveld refinements against both X-ray and time-of-flight neutron diffraction data show that the long-range order of both pyrochlores is described by the cubic space group $Fd\bar{3}m$. Rietveld refinements against data from bank 5 of GEM and high-resolution powder XRD data are shown in Figures 2

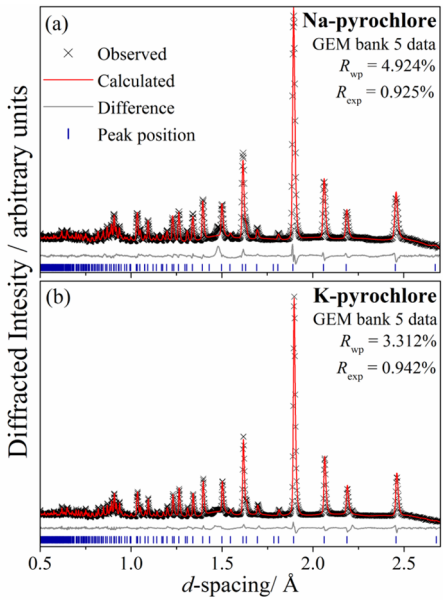

Figure 2. Rietveld refinements against time-of-flight neutron data recorded on detector bank 5 of GEM (mean scattering angle of 92.83° 2θ) using the off-center 96*h* sites and partially occupied 8*b* and 32*e* positions to describe the A and O′ sites of the structure, respectively. Panel (a) shows the Na pyrochlore while panel (b) provides data for the K pyrochlore.

and 3, respectively, and yield compositions of $(Na_{0.60}Bi_{1.40})(Fe_{1.06}Mn_{0.17}Bi_{0.77})O_{6.87}$ and $(K_{0.24}Bi_{1.51})(Fe_{1.07}Mn_{0.15}Bi_{0.78})O_{6.86}$. The elemental ratios obtained from ICP-OES and XRF were used to guide the starting compositions for the Rietveld refinements. Once refined, the compositions agree very well with the values obtained from the bulk analysis (Table 1) with variation of only 1−2% showing that the structural models are a good description of these complex mixed-metal systems. The alkali metals present in the structure occupy the eight-coordinated A site, and satisfactory refinement of the model was only achieved when the remaining bismuth was incorporated onto the octahedral B site. With bismuth excluded from the B site, the intensities of all odd *hkl* reflections were inaccurately modeled. For reasons of both charge balance and size, the bismuth that is upon the B site must be of a higher oxidation state (Bi^{5+}) than that on the A site (Bi^{3+}); the presence of the monovalent alkali metal on the A site requires balancing, and the B site metal is at the center of an octahedral coordination environment much smaller than that of the eight-coordinated A site. Bismuth of different valence mixed across both the A and B sites has been observed previously in a few other bismuth-containing pyrochlore oxides.[11]

The ideal $A_2B_2O_6O'$ pyrochlore structure is highly symmetric and has only one positional parameter to refine, the *x* coordinate of the 48*f* O atom.[1] Refining this ideal model against the X-ray and neutron diffraction data for the new materials yields large anisotropic thermal parameters for the A

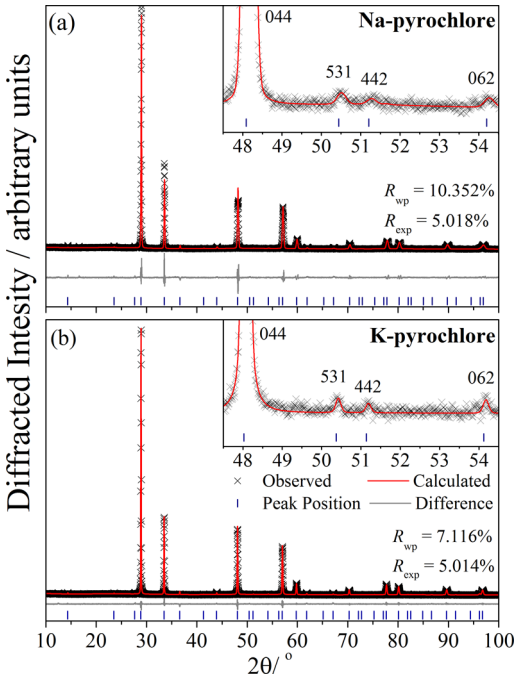

Figure 3. Results from Rietveld refinements against high-resolution powder XRD data that were carried out simultaneously with the neutron refinements for the Na pyrochlore (a) and K pyrochlore (b). The inset in each highlights the small intensity of the 442 reflection that is characteristic of the A-site disorder.

site cations and isotropic thermal parameters of a similar magnitude for the 8*b* O′ site, as shown by Figure 4a. Owing to

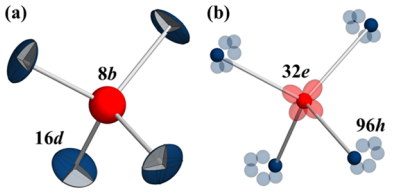

Figure 4. Structural representation of the model produced from Rietveld refinements using (a) the ideal 16*d* site for the A cation, highlighting the large anisotropic and isotropic displacement parameters for the A (16*d*) site and O′ (8*b*) site, respectively. Part (b) shows the results of the refinement when using the 6-fold 96*h* site to model the A cation and the 4-fold 32*e* site that allows the O′ anion to move toward one of the tetrahedral vertices.

the stereochemical activity of the Bi^{3+} lone pair, the A site is likely to have a distorted or asymmetric coordination environment, and as the O′ anions do not form any part of the BO_6 octahedral network and only bridge distances between adjacent A cations, any disorder introduced onto the A site consequently generates disorder in the A_2O' network. The disorder manifests itself in large thermal displacement parameters for the O′ site, the magnitude of which could also be further amplified by the presence of vacancies on this site. Such disorder is often exhibited in pyrochlore systems that contain lone pair active ions such as Sn^{2+} and Bi^{3+}.[2] A more accurate way to model the average structure is to allow the Bi^{3+} cation to be displaced off-center away from the ideal 16*d* site onto the 96*h* site forming a 6-fold symmetrical ring around the ideal site. This has been used previously to model both stoichiometric pyrochlores,[14,31,32] and nonstoichiometric sys-

dx.doi.org/10.1021/ic502411z | Inorg. Chem. 2014, 53, 13197−13206

Table 2. Structural Information Obtained from Rietveld Refinement for Both the Na Pyrochlore and K Pyrochlore Using the Off-Center 96*h* Site To Describe the Eight Coordinate A Site and Partially Occupied 8*b* and 32*e* O′ Positions

atom	site	*x*	*y*	*z*	occupancy	ADPs/Å^2
Na Pyrochlore[a]						
Bi^{III}	96*h*	$^1/_2$	0.521 79(9)	0.478 21(9)	0.1169(4)	*U*11 = 0.0084(15), *U*22 = *U*33 = 0.0145(10), *U*12 = *U*13 = 0.0021(6), *U*23 = −0.0019(10)
Na^{I}	96*h*	$^1/_2$	0.521 79(9)	0.478 21(9)	0.0497(10)	
Fe^{III}	16*c*	0	0	0	0.534(2)	
Mn^{IV}	16*c*	0	0	0	0.086(5)	*U*11 = *U*22 = *U*33 = 0.0040(2), *U*12 = *U*13 = *U*23 = 0.0003(2)
Bi^{V}	16*c*	0	0	0	0.384(2)	
O	48*f*	0.327 70(7)	$^1/_8$	$^1/_8$	1.0000	*U*11 = 0.0151(7), *U*22 = *U*33 = 0.0148(5), *U*23 = 0.0062(7)
O′	8*b*	$^3/_8$	$^3/_8$	$^3/_8$	0.140(5)	*U*11 = *U*22 = *U*33 = 0.013(4)
O′	32*e*	0.3936(3)	0.3936(3)	0.3936(3)	0.1830(14)	*U*11 = *U*22 = *U*33 = 0.025(4), *U*12 = *U*13 = *U*23 = −0.0021(6)
K Pyrochlore[b]						
Bi^{III}	96*h*	$^1/_2$	0.523 29(7)	0.476 71(7)	0.1261(3)	*U*11 = 0.0014(7), *U*22 = *U*33 = 0.0120(6), *U*12 = *U*13 = 0.0007(5), *U*23 = −0.0012(8)
K^{I}	96*h*	$^1/_2$	0.523 29(7)	0.476 71(7)	0.0200(8)	
Fe^{III}	16*c*	0	0	0	0.535(2)	
Mn^{IV}	16*c*	0	0	0	0.075(4)	*U*11 = *U*22 = *U*33 = 0.0037(2), *U*12 = *U*13 = *U*23 = −0.0003(2)
Bi^{V}	16*c*	0	0	0	0.392(2)	
O	48*f*	0.327 04(6)	$^1/_8$	$^1/_8$	1.0000	*U*11 = 0.0160(5), *U*22 = *U*33 = 0.0134(3), *U*23 = 0.0098(4)
O′	8*b*	$^3/_8$	$^3/_8$	$^3/_8$	0.134(4)	*U*11 = *U*22 = *U*33 = 0.011(3)
O′	32*e*	0.3914(3)	0.3914(3)	0.3914(3)	0.1838(13)	*U*11 = *U*22 = *U*33 = 0.048(4), *U*12 = *U*13 = *U*23 = 0.0028(3)

[a] $Fd\bar{3}m$, a = 10.6947(3) Å, $\alpha = \beta = \gamma = 90°$, calculated density = 7.0183(5) g cm^{-3}, R_{wp} = 4.688%, GOF = 3.194. [b] $Fd\bar{3}m$, a = 10.708 49(12) Å, $\alpha = \beta = \gamma = 90°$, calculated density = 7.2007(8) g cm^{-3}, R_{wp} = 3.799%, GOF = 2.506.

tems that contain multiple metals on a single site or metals mixed across both the A and B sites.[12,20,33] Disorder in the A_2O' network can also be modeled by splitting the 8*b* O′ site onto the 4-fold symmetrical 32*e* site that surrounds it, allowing the oxide anion to move closer to one of the coordinating A site cations.[34]

Further evidence for the off-centring of Bi^{3+} is observed through appearance of a weak diffraction feature in the position expected for the 442 crystallographic reflection in the XRD data, highlighted in the insets of Figure 3. Although this is an allowed reflection for space group $Fd\bar{3}m$, for cubic pyrochlores in which the A cation is on the ideal 16*d* site, this reflection has negligible or zero intensity. The appearance of this peak can be explained by the displacement of the Bi^{3+} ion toward the surrounding O ions and away from this ideal site onto a lower symmetry position such as the 96*h*.[32,35,36]

Rietveld refinements against the XRD and neutron data produced slightly improved fits when the bismuth and alkali metals were allowed to be displaced onto the 96*h* positions. Fits with off-centering gave R_{wp} = 4.826% and 3.890% for the Na and K pyrochlores, respectively, compared with R_{wp} = 5.071% and 4.014% when the metals were confined to the ideal 16d site. As expected the shift of the A site cations off-center dramatically reduces their anisotropic displacement parameters (ADPs); however, the thermal parameters for the 8*b* O′ still remain larger than expected. Allowing some of the O′ atoms to displace away from the 8*b* position by refining the occupancy of the tetrahedral 32*e* site improves the fit slightly, giving R_{wp} = 4.688% for the Na pyrochlore and R_{wp} = 3.799% for the K pyrochlore. The magnitude of the thermal parameters for the 8*b* sites are reduced 5-fold, and the ADPs for the 32*e* sites result in slightly elongated thermal ellipsoids directed toward the coordinating A site atom, as seen in Figure 4b. Comparison of this model which has the O′ atoms spread across both the 8*b* and 32*e* positions with a model where all of the O′ atoms are displaced onto the 32*e* site shows insignificant difference between the refinements and thermal parameters obtained. As the A site is partially occupied with the alkali metal, which unlike Bi^{3+} has no lone pair to drive static displacements, the mixed O′ 8*b*/32*e* model is the more realistic solution as the coordination environments of Bi^{3+} and Na^+/K^+ are not alike.

The A site is slightly deficient for the K pyrochlore, and the refined potassium content is much lower compared to the sodium content of the Na pyrochlore. Though the Bi^{3+} cation would not reside in symmetrical coordination, its tabulated ionic radius is 1.17 Å,[30] almost identical to that of Na^+ (1.18 Å) so it is likely that the introduction of K^+ (1.51 Å) into the structure causes an expansion of the lattice. There is a much greater difference between the ionic radii of Bi^{3+} and K^+ than for Bi^{3+} and Na^+, and it could be that cation size variance effects produce a solubility limit for potassium on the A site of the structure. The lattice parameter of the K pyrochlore is affected by the K^+ content, and as mentioned above, it is slightly larger even with the reduced amount of potassium compared to sodium. It could be that a combination of both size variance and expansion of the lattice limits the solubility of K^+ within the structure. Vacancies can be accommodated on the A site of the pyrochlore structure, and partial occupation is common in many systems.[1,5] The occupancy of the A site for the K pyrochlore, equal to 0.8766, is almost the same as the occupancy of the O′ site (0.8688) once multiplicity is taken into account. These deficiencies are likely to be related as both sites are part of the A_2O' network; however, this effect is not observed for the Na pyrochlore which has a fully occupied A site and a slightly vacant O′ site.

The structural details obtained from Rietveld refinements of both pyrochlores are listed in Table 2, along with various measures of the fit quality. For comparison, the results from refinements that use the ideal 16*d* position and the off-center 96*h* position (without 32*e* O′) to describe the pyrochlore structures are provided in the Supporting Information (Tables S1 and S2). The resulting structures for both pyrochlores are rather similar. The displacement of the A site cation away from the ideal 16*d* position is 0.3296(5) Å for the Na pyrochlore and 0.3280(6) Å for the K pyrochlore, while the 32*e* O′ site is displaced from the ideal 8*b* position toward the coordinating A

dx.doi.org/10.1021/ic502411z | Inorg. Chem. 2014, 53, 13197−13206

site atoms by 0.3446(8) and 0.3314(8) Å for the Na and K pyrochlore, respectively.

The measured densities of the Na and K pyrochlores are very similar and agree well with the densities calculated from the refined crystal structures. For the Na pyrochlore the values are almost identical with a crystallographic density of 7.018 g cm^{-3} and experimentally determined value of 7.064 g cm^{-3} while for the potassium analogue the calculated and experimental values are 7.201 and 7.094 g cm^{-3}, respectively. Though the powders were heated prior to measurement to drive off any residual moisture, these small discrepancies could be due to the presence of some surface water that results in slight inaccuracies in the pycnometry results.

With regards to the potential for the materials to contain structural water, an excess of oxygen is observed on the 8*b* O′ site when considering the balance of charge from the four different metals. Excess oxygen on this site could be due to structural water or hydroxide ions, as seen in other pyrochlores, with the hydrogen atoms being located approximately 1 Å away on the 32*e* site.[37] The thermal behavior of the K pyrochlore under air is illustrated in Figure 5 through *in situ* XRD data and

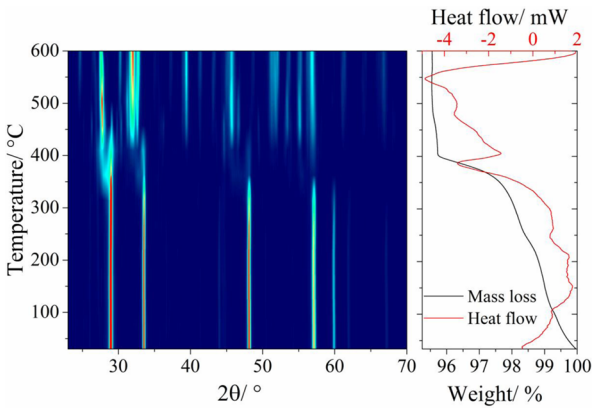

Figure 5. Thermal behavior of the K pyrochlore from room temperature up to 600 °C. The left panel displays a contour plot of powder XRD data showing how the pyrochlore phase decomposes in to a mixture of sillenite ($Bi_{12}MnO_{20}$) and bismuth ferrite ($BiFeO_3$). The TGA plot shows the corresponding mass loss for this decomposition with the DSC trace providing an accurate endothermic decomposition temperature of 386.7 °C.

TGA-DSC curves, with the data for the Na pyrochlore provided in the Supporting Information (Figure S3). The TGA data show a gradual loss of water up to the point where each pyrochlore breaks down. The mass loss from 80 °C (the temperature at which the samples were heated prior to measurement in the neutron beam) up to the decomposition temperature of around 395 °C corresponds to a number of water molecules equivalent to the excess oxygen on the O′ site. For example the O′ site in the Na pyrochlore is overoccupied by 0.61, and the mass loss from 80 °C up to the decomposition temperature corresponds to 0.63 mol of H_2O. Attempts at trying to introduce crystal water into structural refinements, however, proved unsuccessful. When placing the hydrogen/deuterium on the 32*e* site, as in previous reports, the quality of the fit to the data is not improved and the occupancy of the site always refines down to negligible amounts. The presence of water is, however, observed through infrared (IR) spectroscopy, shown in Supporting Information Figure S4. The typical broad O−H stretching mode in the region of ca. 3300 cm^{-1} is evidence of water or hydroxide, as is the sharper vibrational mode observed at ca. 1637 cm^{-1} that corresponds to the H−O−H bending mode of water, consistent with spectra recorded from various other hydrated pyrochlores.[38] The powders were heated to 80 °C before further IR spectra were recorded to determine whether these observed modes correspond to surface water or water within the crystal structure. After this drying, the observed modes disappeared suggesting that they belong mostly to moisture coordinated to the surface of the powders, but given the sharpness of the IR band, the presence of crystal water cannot be ruled out by this technique.

Both pyrochlores are metastable and break down at comparable decomposition temperatures to give similar products. The endothermic peak observed in the DSC curve corresponding to the decomposition occurs at a temperature of 387 °C for the K pyrochlore and 403 °C for the Na pyrochlore. As they begin to break down, *in situ* powder XRD, Figure 5, shows initially the development of weak shoulders on the 222, 004, 044, and 622 Bragg reflections at slightly higher *d*-spacings than those of the pyrochlore. The peak positions of these shoulders match those of the cubic fluorite δ-Bi_2O_3, a phase which is usually only stable above 730 °C,[39] but may be stabilized at considerably lower temperature when doped with another metal. However, as these reflections are very low intensity and overlap with those of the pyrochlore, it is not possible to assign them to a fluorite-type phase with complete certainty. The pyrochlore continues to decompose with the simultaneous formation of sillenite (a mix of both $Bi_{12}MnO_{20}$ and $Bi_{25}FeO_{40}$) and $BiFeO_3$ over the range 400−450 °C. Above 500 °C the $Bi_{25}FeO_{40}$ disappears as $BiFeO_3$ crystallizes further, suggesting that the iron sillenite is a kinetic intermediate and bismuth ferrite is the thermodynamic product from the decomposition. The remaining sillenite peak positions agree with those of $Bi_{12}MnO_{20}$.[40]

X-ray absorption near-edge spectroscopy (XANES) was used to determine the oxidation states of the metals in the two pyrochlores, as seen in Figure 6. From comparison with reference materials, the edge positions of the pyrochlore samples for the Mn K-edge spectra are similar to that of the rutile-structured MnO_2, suggesting the presence of octahedral Mn^{4+}. The Fe K-edge spectra have edge positions for both pyrochlore materials that are shifted to slightly higher energies than the Fe^{3+} references, but it should be borne in mind that XANES analyses performed at the K-edges can be sensitive to the local coordination environment of the target metal as well as its oxidation state. This would be consistent with the expected difference in local coordination environments between the pyrochlores and both α-Fe_2O_3 and $BiFeO_3$.

A pre-edge feature at ca. 7.114 keV in the Fe K-edge XANES is due to the 1s−3d transition, characteristic of local environments with reduced symmetry, as seen in the spectrum for Fe_3O_4 which adopts a spinel-type structure with some Fe^{3+} coordinated in a tetrahedral environment. The absence of any such feature in both the Mn and Fe K-edge spectra of our pyrochlores confirms that the transition metals have an octahedral coordination, agreeing with the refinements made against X-ray and neutron powder diffraction data. Another possibility to account for the difference between the XANES of the pyrochlores and the Fe^{3+} reference materials is that small amounts of iron are present on the A site, a common trait of disordered transition metal pyrochlores.[4,19,20] However, refinements of models containing small amounts of iron on the A site against the X-ray and neutron data gave no improvement or

dx.doi.org/10.1021/ic502411z | *Inorg. Chem.* 2014, 53, 13197−13206

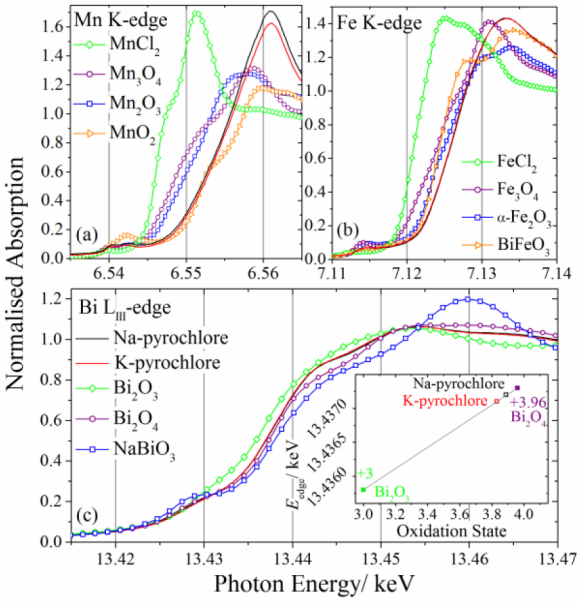

Figure 6. XANES spectra of the pyrochlores compared to those of reference materials at the (a) Mn K-edge, (b) Fe K-edge, and (c) the Bi L_{III}-edge. The Na and K pyrochlores are represented by black and red lines, respectively, and references are shown as data point-lines. The inset in part (c) shows a plot of edge shift against oxidation state determined using the reference materials (colored squares). The Na and K pyrochlore are marked on the line using hollow black and red squares, respectively, giving bismuth oxidation states of +3.89 and +3.83.

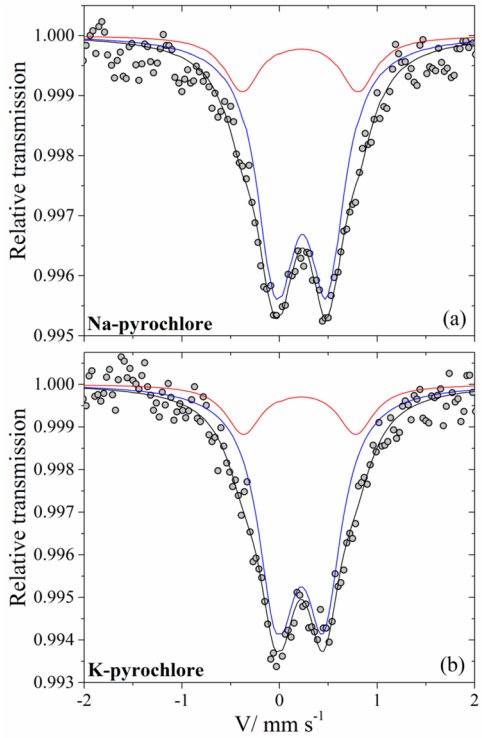

Figure 7. Transmission ^{57}Fe Mössbauer spectra of the (a) Na pyrochlore and (b) K pyrochlore recorded at 300 K showing two-component fit (black, blue, and red lines) to the data (gray open points).

reduction to the quality of the refinements, and therefore did not present a clear conclusion on the possibility of A site Fe (see Supporting Information Table S3).

Transmission ^{57}Fe Mössbauer spectrometry was used to further investigate the local Fe environment. The spectra recorded at 300 K for both pyrochlores are shown in Figure 7. The relatively low statistics of the observed data are due to the high content of absorbing Bi in these pyrochlores. The spectra measured at 300 and 77 K both exhibit a symmetrical quadrupolar doublet with broadened lines. The spectra for each pyrochlore are almost identical, and the quadrupolar isomer shifts (δ) are consistent with the presence of Fe^{3+} situated within octahedral units in a high-spin state configuration, showing no evidence for the presence of other species in different coordination environments. The hyperfine structural details are provided in Table 3 and show that the two components have very different quadrupolar splittings, though they are very similar for both pyrochlores. Using a single doublet component to fit the spectrum did not accurately reproduce the profile, while using two quadrupolar components allows the line shape to be satisfactorily modeled. The same situation has been reported previously for other Fe containing pyrochlores, such as $(Bi_{1.8}Fe_{0.2})(FeSb)O_7$ and $Bi_2BB'O_7$ (where B = Cr or Fe, and B′ = Nb, Ta, and Sb).[41] These studies concluded that the two observed components were due to small amounts of iron that were located on the A site with the majority on the B site of the structure; however, in the current study the two component fit to the Mössbauer data could equally be due to the presence of chemical disorder in the crystal structure. Three cations of different oxidation state and radius occupying the B site (ionic radii of high-spin Fe^{3+}, Mn^{4+}, and Bi^{5+} are 0.645, 0.53, and 0.76 Å, respectively) introduce static disorder into the local environment, which also explains the rather large line widths that are observed.

The XANES spectra recorded at the Bi L_{III}-edge are displayed in panel c of Figure 6. Comparison with the reference samples shows that the pyrochlores do contain Bi^{3+} and Bi^{5+} akin to other mixed-valence bismuth-containing pyrochlores.[11] The shape of the near edge region of the pyrochlore materials and also the immediate postedge region are very similar to that of Bi_2O_4, in which Bi^{5+} occupies a regular octahedron, while Bi^{3+} is in an irregular cubic, eight-coordinated environment comparable to the structure of the pyrochlores. The Bi_2O_4 reference was synthesized hydrothermally following the method of Kumada et al.,[42] (Supporting Information Figure S5) and the powder produced, like that of Kumada et al., was not entirely phase pure and contained a small amount (3.35%) of the high-temperature phase of δ-Bi_2O_3, giving an average oxidation state of +3.96 for the reference material. The average oxidation states of Bi in the Na and K pyrochlores are determined from the XANES (Figure 5c, inset) to be +3.89 and +3.83, respectively, agreeing well with the results from structure refinement by showing that there is more Bi^{3+} than Bi^{5+} present. The slightly lower oxidation state observed for the K pyrochlore is also consistent with the Rietveld result.

Observation of samples of both pyrochlore materials under an electron microscope shows that the crystallites are octahedral in shape and have a fairly wide size distribution. Transmission electron microscopy (TEM), shown in Figure 8a, shows how these crystals are agglomerated. High resolution TEM images (Figure 8b) show the clean edges and a vertex typical of octahedral crystals. It is demonstrated more distinctly however by scanning electron microscopy (SEM) in Figure 8c

dx.doi.org/10.1021/ic502411z | Inorg. Chem. 2014, 53, 13197−13206

Table 3. Results from the Fitting of ^{57}Fe Mössbauer Spectra

	isomer shift (δ)/mm s^{-1}	linewidth (Γ)/mm s^{-1}	quadrupolar splitting (Δ)/mm s^{-1}	contribution/%
Na Pyrochlore				
Fe 1	0.33(1)	0.44(2)	1.12(2)	19(2)
Fe 2	0.33(1)	0.44(2)	0.45(2)	81(2)
K Pyrochlore				
Fe 1	0.34(1)	0.44(2)	1.16(2)	19(2)
Fe 2	0.35(1)	0.44(2)	0.50(2)	81(2)

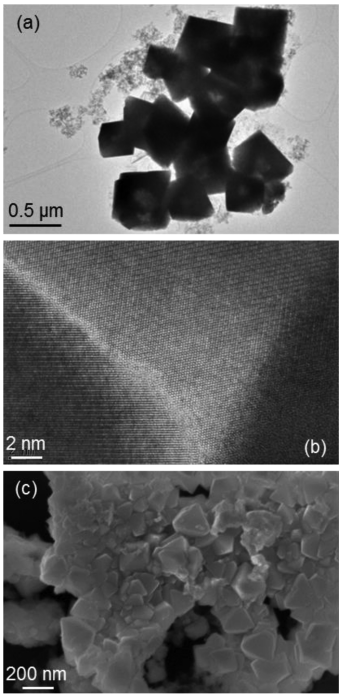

Figure 8. Transmission electron microscopy (TEM) (a) image of agglomerated crystallites of the pyrochlore phase with octahedral type morphologies, and (b) a high-resolution image of a single crystallite focused on a vertex and edges of the octahedral shaped crystal. Scanning electron microscopy (SEM) (c) reveals that the crystallites are not clustered, but are in fact crystallized together.

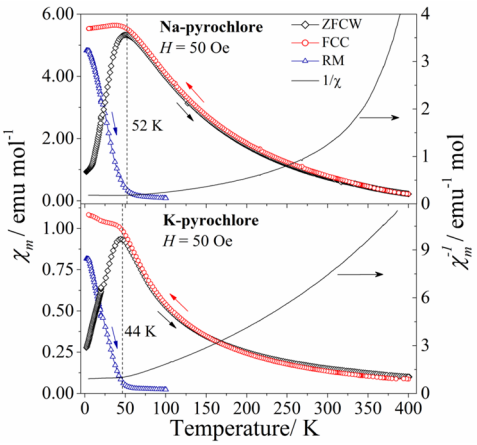

Figure 9. Magnetic susceptibility vs temperature measured in an applied field of 50 Oe for both the Na and K pyrochlore with zero field-cooled warming (ZFCW) curves shown by red circles, field-cooled cooling curves (FCC) shown by black diamonds, and remanent magnetization (RM) data measured up to 100 K shown by blue triangles. The inverse susceptibility curves (shown as black lines) correspond to the right-hand axis. The irreversibility temperature (see text) is marked by the vertical dashed line.

that the crystallites are not merely agglomerated, but actually appear to crystallize and grow from one another, and therefore make up large particles that appear as clusters of several smaller crystallites.

Magnetism. Both of the transition metals in the pyrochlores studied have a magnetic moment, with Fe^{3+} and Mn^{4+} having electron configurations of $3d^5$ and $3d^3$, respectively, which likely will contribute differently to any magnetic interactions. The magnetic susceptibility for each pyrochlore, measured in an applied field of 50 Oe as a function of temperature, is shown in Figure 9, including zero field-cooled warming (ZFCW), field-cooled cooling (FCC), and remanent magnetization (RM) curves and also the inverse susceptibility. For both pyrochlores the ZFCW data deviate from the FCC data at low temperature: at 52 K for the Na pyrochlore and 44 K for the K pyrochlore. The point of deviation has previously been labeled as the irreversibility temperature and is a characteristic feature of spin-glass materials.[20,43] The RM curves show data collected on warming from 2 to 100 K in zero-field after the powder was cooled in the applied field of 50 Oe. Under these conditions the magnitude of the measured susceptibility rapidly decreases and reaches zero at the temperature corresponding to the divergence of the ZFCW and FCC curves. This supports the notion of the irreversibility temperature associated with frustrated systems and is indicative of magnetic interactions occurring below this temperature. The inverse susceptibility data do not follow Curie–Weiss behavior at higher temperatures than this, and with no linear region to fit it is not possible to determine an effective moment for each pyrochlore. Though this suggests that there is no long-range magnetic ordering, the observed low temperature behavior implies that the magnetic B site cations could exhibit some coupling interactions, rather than behaving as independent paramagnetic ions that follow the Curie–Weiss law. Heat capacity measurements are consistent with this notion as there are no observed features in the specific heat data leading to the conclusion that these materials lack long-range magnetic order (Supporting Information Figure S6). Frustrated low-temperature magnetic behavior is commonly observed in pyrochlores and is a property inherent to the cation sublattice due to the tetrahedral nature of the metal positions. It is likely that the disorder present in our materials, resulting from multiple metals occupying the same crystallographic sites as well as disorder from stereochemical cations, further contributes to the observed frustrated magnetic behavior.

The irreversibility temperature, sometimes referred to as the freezing temperature, has been associated with competing interactions between magnetically ordered clusters or spins, and it is this which results in the spin-glass-like state.[20] For our pyrochlores, the interactions that occur below this temperature will depend strongly upon the number of next nearest

dx.doi.org/10.1021/ic502411z | Inorg. Chem. 2014, 53, 13197–13206

neighbors that are magnetic, especially as 40% of the B site is also shared by nonmagnetic Bi^{5+}. It has been shown in other pyrochlores, such as $(Bi_{1.89}Fe_{0.11})(Fe_{1.05}Nb_{0.95})O_7$ and $(Bi_{1.88}Fe_{0.12})(Fe_{1.42}Te_{0.58})O_{6.87}$, that this irreversibility temperature, characteristic of a spin-freezing transition, is dependent upon the magnitude of the applied external magnetic field, with the irreversibility temperature decreasing as a greater magnetic field is applied.[20,36] Those particular pyrochlore materials were said to lack long-range order due to the irreversibility temperature shifting to lower values with increasing field. The effect of increasing the magnetic field on the irreversibility temperature for both pyrochlores we have prepared is shown in Figure 10, which shows that the temperature at which the

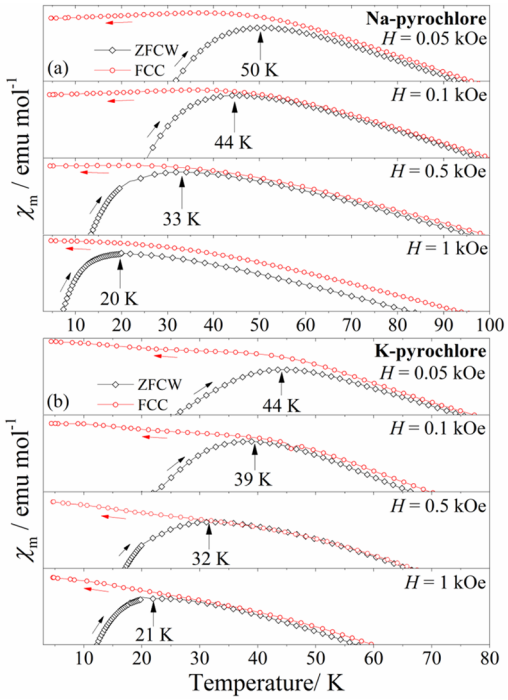

Figure 10. Variation in magnetic susceptibility and irreversibility temperature, defined as the point at which ZFCW and FCC data diverge, with increasing fields for both the (a) Na and (b) K pyrochlores. The decrease in irreversibility temperature toward 0 K with increasing applied field is a phenomenon typical to frustrated glassy-type magnetic systems.

ZFCW and FCC curves converge decreases as the applied magnetic field increases, further supporting our conclusion that they exhibit spin-glass-like behavior rather than long-range magnetic order. When the applied field is sufficiently large ($H >$ 10 kOe) the divergence of the ZFCW and FCC curves is no longer observed due to the saturation of the magnetization in the spin glass state.

Magnetization measurements recorded as a function of applied field at 10 K, shown in Figure 11, highlight a very weak hysteresis in both pyrochlores each with a coercive field of ca. 250 Oe, showing that the pyrochlores are relatively soft magnetic materials. The remanent magnetization for the Na pyrochlore is approximately double that of the K- pyrochlore. Also of note is that the magnetization of the Na pyrochlore becomes saturated in an applied field approximately half the magnitude of that required to saturate the K pyrochlore. A similar distinction between the two pyrochlores is observed in the shift of irreversibility temperature (Figure 10) where

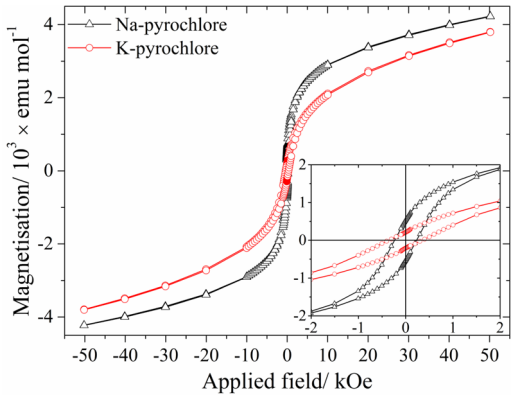

Figure 11. Variation in magnetization for both pyrochlores as a function of applied field up to 50 kOe measured at 10 K. The inset highlights the weak hysteresis observed in both systems.

identical fields were used but the temperature shift observed for the Na pyrochlore is larger than that for the K pyrochlore.

CONCLUSIONS

The direct hydrothermal synthesis of two new complex pyrochlores has been reported. These metastable pyrochlores decompose at ca. 395 °C and would therefore not be accessible via conventional (high temperature) solid-state synthetic routes. We show that the overall average structures of these systems are described by the cubic space group $Fd\bar{3}m$, and are accurately modeled when the A site atoms and O′ oxygen are displaced away from the ideal sites onto lower symmetry positions, an effect likely driven by the active lone pair on Bi^{3+} as seen in other related pyrochlore materials. Our structural analysis also reveals the presence of considerable static disorder caused by the presence on the B site of three different metals of varying oxidation states, as shown by XANES. The magnetic properties of the materials are probed and suggest that spin-glass-like behavior is adopted rather than long-range magnetic ordering which is a common characteristic of many geometrically frustrated pyrochlore systems.

ASSOCIATED CONTENT

Supporting Information

Further details are provided on the synthesis involving ammonia (Figure S1), results from Rietveld refinement against banks 3 and 4 of GEM (Figure S2), structural results from using the ideal pyrochlore structure (Tables S1−S3), thermal behavior and IR spectra (Figures S3 and S4, respectively), and XANES of reference materials (Figure S5). Results of specific heat measurements (Figure S6). This material is available free of charge via the Internet at http://pubs.acs.org.

AUTHOR INFORMATION

Corresponding Author

*E-mail: r.i.walton@warwick.ac.uk.

Notes

The authors declare no competing financial interest.

ACKNOWLEDGMENTS

We thank the EPSRC and the STFC Centre for Materials Physics and Chemistry for cofunding the studentship of L.M.D. (CMPC11104). L.M.D. thanks Dr. Andrew Grigg for his assistance with the analysis of time-of-flight neutron data in

TOPAS-Academic. Dr. Reza Jalilikashtiban is thanked for the TEM imaging. Dr. Martin Lees also is thanked for the measurement of heat capacity data. Some of the instruments used at the University of Warwick were obtained through the Science City Advanced Materials project "Creating and Characterizing Next Generation Advanced Materials" with support from Advantage West Midlands (AWM) and partially funded by the European Regional Development Fund (ERDF).

REFERENCES

(1) Subramanian, M. A.; Aravamudan, G.; Rao, G. V. S. *Prog. Solid State Chem.* **1983**, *15*, 55−143.
(2) Weller, M. T.; Hughes, R. W.; Rooke, J.; Knee, C. S.; Reading, J. *Dalton Trans.* **2004**, 3032−3041.
(3) Vanderah, T. A.; Levin, I.; Lufaso, M. W. *Eur. J. Inorg. Chem.* **2005**, *2005*, 2895−2901.
(4) Zhou, Q.; Blanchard, P. E. R.; Kennedy, B. J.; Ling, C. D.; Liu, S.; Avdeev, M.; Aitken, J. B.; Tadich, A.; Brand, H. E. A. *J. Alloys Compd.* **2014**, *589*, 425−430.
(5) Modeshia, D. R.; Walton, R. I. *Chem. Soc. Rev.* **2010**, *39*, 4303−4325.
(6) Lewandowski, J. T.; Pickering, I. J.; Jacobson, A. J. *Mater. Res. Bull.* **1992**, *27*, 981−988.
(7) Wright, C. S.; Fisher, J.; Thompsett, D.; Walton, R. I. *Angew. Chem., Int. Ed.* **2006**, *45*, 2442−2446. Nyman, M.; Rodriguez, M. A.; Shea-Rohwer, L. E.; Martin, J. E.; Provencio, P. P. *J. Am. Chem. Soc.* **2009**, *131*, 11652−11653.
(8) Sardar, K.; Walton, R. I. *J. Solid State Chem.* **2012**, *189*, 32−37.
(9) Dong, Q.; Jiang, H.; Kumada, N.; Yonesaki, Y.; Takei, T.; Kinomura, N. *J. Solid State Chem.* **2011**, *184*, 1899−1902.
(10) Mao, Y.; Li, G.; Xu, W.; Feng, S. *J. Mater. Chem.* **2000**, *10*, 479−482.
(11) Trehoux, J.; Abraham, F.; Thomas, D.; Doremieux-Morin, C.; Arribart, H. *J. Solid State Chem.* **1988**, *73*, 80−91. Kumada, N.; Hosoda, M.; Kinomura, N. *J. Solid State Chem.* **1993**, *106*, 476−484. Kinomura, N.; Hosoda, M.; Kumada, N.; Kojima, H. *J. Ceram. Soc. Jpn.* **1993**, *963*, 966−968.
(12) Zhou, Q.; Kennedy, B. J.; Ting, V.; Withers, R. L. *J. Solid State Chem.* **2005**, *178*, 1575−1579.
(13) Wu, W.; Fumoto, K.; Oishi, Y.; Okuyama, M.; Hamakawa, Y. *Jpn. J. Appl. Phys.* **1996**, *35*, 1560−1563.
(14) Hector, A. L.; Wiggin, S. B. *J. Solid State Chem.* **2004**, *177*, 139−145.
(15) Withers, R. L.; Welberry, T. R.; Larsson, A.; Liu, Y.; Norén, L.; Rundlöf, H.; Brink, F. J. *J. Solid State Chem.* **2004**, *177*, 231−244.
(16) Melot, B.; Rodriguez, E.; Proffen, T.; Hayward, M. A.; Seshadri, R. *Mater. Res. Bull.* **2006**, *41*, 961−966.
(17) Liu, Y.; Withers, R. L.; Welberry, T. R.; Wang, H.; Du, H.-L.; Yao, X. *J. Electroceram.* **2008**, *21*, 401−404.
(18) Krayzman, V.; Levin, I.; Woicik, J. C. *Chem. Mater.* **2007**, *41*, 932−936.
(19) Babu, G. S.; Bedanta, S.; Valant, M. *Solid State Commun.* **2013**, *158*, 51−53.
(20) Miiller, W.; Causeret, L.; Ling, C. D. *J. Phys.: Condens. Matter* **2010**, *22*, 486004−486010.
(21) Chen, C.; Cheng, J.; Yu, S.; Che, L.; Meng, Z. *J. Cryst. Growth* **2006**, *291*, 135−139.
(22) Smirnova, O.; Azuma, M.; Kumada, N.; Kusano, Y.; Matsuda, M.; Shimkawa, Y.; Takei, T.; Yonesaki, Y.; Kinomura, N. *J. Am. Chem. Soc.* **2009**, *131*, 8313−8317.
(23) Hannon, A. C. *Nucl. Instrum. Methods Phys. Res., Sect. A* **2005**, *551*, 88−107.
(24) Soper, A. K. *Rutherford Appleton Laboratory Technical Report RAL-TR-2011-013*; 2011.
(25) Coelho, A. A. *J. Appl. Crystallogr.* **2000**, *33*, 899−908.
(26) Williams, W. G.; Ibberson, R. M.; Day, P.; Enderby, J. E. *Physica B* **1998**, *241*, 234−236.
(27) Dent, A. J.; Cibin, G.; Ramos, S.; Smith, A. D.; Scott, S. M.; Varandas, L.; Pearson, M. R.; Krumpa, N. A.; Jones, C. P.; Robbins, P. E. *J. Phys.: Conf. Ser.* **2009**, *190*, 012039−012042.
(28) Ravel, B.; Newville, M. *J. Synchrotron Radiat.* **2005**, *12*, 537−541.
(29) Varret, F.; Teillet, J. *MOSFIT Program*; 1976, unpublished.
(30) Shannon, R. D. *Acta Crystallogr., Sect. A* **1976**, *32*, 751−767.
(31) Jones, R. H.; Knight, K. S. *J. Chem. Soc., Dalton Trans.* **1997**, 2551−2555.
(32) Henderson, S. J.; Shebanova, O.; Hector, A. L.; McMillan, P. F.; Weller, M. T. *Chem. Mater.* **2007**, *19*, 1712−1722.
(33) Vanderah, T. A.; Siegrist, T.; Lufaso, M. W.; Yeager, M. C.; Roth, R. S.; Nino, J. C.; Yates, S. *Eur. J. Inorg. Chem.* **2006**, *2006*, 4908−4914.
(34) Lufaso, M. W.; Vanderah, T. A.; Pazos, I. M.; Levin, I.; Roth, R. S.; Nino, J. C.; Provenzano, V.; Schenck, P. K. *J. Solid State Chem.* **2006**, *179*, 3900−3910. Nguyen, H. B.; Norén, L.; Liu, Y.; Withers, R. L.; Wei, X.; Elcombe, M. M. *J. Solid State Chem.* **2007**, *180*, 2558−2565.
(35) Levin, I.; Amos, T. G.; Nino, J. C.; Vanderah, T. A.; Randall, C. A.; Lanagan, M. T. *J. Solid State Chem.* **2002**, *168*, 69−75.
(36) Babu, G. S.; Valant, M.; Page, K.; Llobet, A.; Kolodiazhnyi, T.; Axelsson, A.-K. *Chem. Mater.* **2011**, *23*, 2619−2625.
(37) Dickens, P. G.; Weller, M. T. *Solid State Commun.* **1986**, *59*, 569−573. Sardar, K.; Fisher, J.; Thompsett, D.; Lees, M. R.; Clarkson, G. J.; Sloan, J.; Kashtiban, R. J.; Walton, R. I. *Chem. Sci.* **2011**, *2*, 1573−1578.
(38) Perottoni, C. A.; Haines, J.; da Jornada, J. A. H. *J. Solid State Chem.* **1998**, *141*, 537−545. Goh, G. K. L.; Levi, C. G.; Lange, F. F. *J. Mater. Res.* **2002**, *17*, 3168−3176.
(39) Sammes, N. M.; Tompsett, G. A.; Näfe, H.; Aldinger, F. *J. Eur. Ceram. Soc.* **1999**, *19*, 1801−1826.
(40) Delicat, U.; Radaev, S. F.; Trömel, M.; Behrens, P.; Kargin, Y. F.; Mar'in, A. A. *J. Solid State Chem.* **1994**, *110*, 66−69.
(41) Egorysheva, A. V.; Ellert, O. G.; Maksimov, Y. V.; Volodin, V. D.; Efimov, N. N.; Novotortsev, V. M. *J. Alloys Compd.* **2013**, *579*, 311−314. Blanco, M. C.; Franco, D. G.; Jalit, Y.; Pannunzio Miner, E. V.; Berndt, G.; Paesano, A., Jr.; Nieva, G.; Carbonio, R. E. *Physica B* **2012**, *407*, 3078−3080.
(42) Kumada, N.; Kinomura, N.; Woodward, P. M.; Sleight, A. W. *J. Solid State Chem.* **1995**, *116*, 281−285.
(43) Filoti, G.; Rosenberg, M.; Kuncser, V.; Seling, B.; Fries, T.; Spies, A.; Kemmler-Sack, S. *J. Alloys Compd.* **1998**, *268*, 16−21.